CrossMark

Parametric Evolution of Power-law Energy Spectra of Energetic Electrons in the Coronal Loops

Jian-Fei Tang[1,2], De-Jin Wu[2], Ling Chen[2], and Lei Xu[3]

[1] College of Engineering and Design, Lishui University, Lishui 323000, China; tjf1027@163.com
[2] Key Laboratory of Planetary Sciences, Purple Mountain Observatory, CAS, Nanjing 210023, China
[3] School of Physics and Electronic Information, Shangrao Normal University, Shangrao 334001, China

Abstract

Fast electron beams (FEBs) are one of the main products of various active events and are ubiquitous in solar, space and cosmic plasmas. They reveal themselves in hard X-ray and radio emissions. The observed characteristics of X-ray and radio emissions sensitively depend on the energy distribution of FEBs, which usually have a power-law energy spectrum. As FEBs travel in the solar atmosphere, their energy distribution can considerably vary due to the interaction with ambient plasmas. Tang et al. investigated the evolution of the energy spectrum of the FEBs traveling along a flare loop and discussed the possible effects on associated hard X-ray (HXR) and radio emissions. Considering the ubiquitous coronal loops in active regions, in the present paper, we investigate the parametric evolution of the energy spectra of FEBs when propagating along coronal loops. Here, we take the sunpot atmospheric model as an approximate coronal loop atmosphere model. The results show that the energy loss has an important impact on the cutoff behavior and energy spectra of FEBs when precipitating in a coronal loop with density ratio $n_b/n_e = 0.01$. The initially single power-law spectrum with a steepness cutoff can evolve into a more complex double power-law spectrum or two "knees" power-law spectrum with a flattened steepness cutoff behavior or saturation cutoff behavior. Our calculations also demonstrate that the energy spectrum evolution is not obvious if $n_b/n_0 = 0.001$ as Tang et al. asserted. The present results are helpful for a more comprehensive understanding of the dynamic spectra of HXR and radio emissions from FEBs.

Key words: Sun: activity – Sun: flares – Sun: radio radiation

1. Introduction

Based on its high resolution and large field of view, the Transition Region and Coronal Explorer (TRACE) has obtained some excellent extreme ultraviolet (EUV) images and movies. These observations have changed our understanding of the corona, especially of active regions, which appear to be made entirely by loop structures (Del Zanna & Mason 2003). Although coronal loops have been well defined and studied in the EUV band, we should still be aware that most coronal loops are also visible in X-ray band. So when observed with X-ray spectroscopy, the whole X-ray bright corona also consists of magnetic loops. Coronal loops are magnetic structures with an approximate semicircular shape, which are filled with hot and dense plasma. They generally originate in strong unipolar regions and end up in either different active regions or connect two polarities across a neutral line (Schrijver et al. 1999). According to the length of coronal loops, they can be divided into bright points ($\sim 10^8$ cm), active region loops (10^9–10^{10} cm) and giant arches ($\sim 10^{11}$ cm) (Reale 2010). The fully ionized plasma is confined in the coronal loops and isolated from the ambient plasma. Such magnetized plasma is well insulated because it conducts most

of the thermal energy along the magnetic field. Thus, coronal loops have different temperatures and can be roughly divided into cold loops ($\sim 10^5$ K), X-ray loops (to a few 10^6 K) and flaring loops (up to a few 10^7 K) (Reale 2010). The typical values of the plasma density of coronal loops are 10^9–10^{10} cm^{-3}, while flare loops have densities of at least one order of magnitude denser (Reale 2010). In this paper, "coronal loops" are defined as X-ray loops with typical density of 10^9–10^{10} cm^{-3} and temperature of a few 10^6 K, excluding flare loops.

Accelerated electrons are ubiquitous in space and cosmic plasmas (Narukage et al. 2014). For the Sun, there are several mechanisms for electron acceleration: magnetic reconnection, coronal shock waves, and even the interaction between coronal mass ejection and the background magnetized plasma loops (Tan et al. 2019). During a flare, enormous magnetic energy is suddenly released and transferred partly into the thermal and kinetic energies of energetic particles such as electrons, protons and heavy ions (Masuda et al. 1994; Yokoyama et al. 2001; Hara et al. 2011; Imada et al. 2013). These flare accelerated electrons travel along solar magnetic fields and form fast electron beams (FEBs). They can be inferred from their excited

radio bursts and hard X-ray (HXR) bursts when they propagate in the solar atmosphere (Lin & Schwartz 1987; Dulk et al. 1992; Holman et al. 2011), and even can be detected directly by particle detectors when FEBs travel into near-Earth interplanetary space (Lin 2011). It is believed that FEBs propagate downward along the magnetic field, and the small pitch angles precipitating electrons will hit the denser chromosphere and excite HXR emissions via bremsstrahlung (Aschwanden et al. 1995). So, X-ray radiation is a more direct window which provides important information on acceleration and transportation processes of the FEBs. Flare HXR observations show that there are usually a corona source and two footpoint sources in the chromosphere. The standard HXR emission model involves the thin-target bremsstrahlung in the corona source and the thick-target bremsstrahlung in the footpoint sources. In this standard model, power-law FEBs $F_0(E) \propto E^{-\delta}$ will emit HXR with spectra $I_{tp}(\epsilon) \propto \epsilon^{-\gamma_{tp}}$ via the thin-target bremsstrahlung in the corona source, here $\gamma_{tp} = \delta + 1$ is the photon spectral index (Holt & Cline 1968; Syrovatskii & Shmeleva 1972; Lin & Hudson 1976; Hannah & Kontar 2011). If the FEBs do not lose energy, they will produce HXR spectra $I_{ft}(\epsilon) \propto \epsilon^{-\gamma_{ft}}$ via the thick-target bremsstrahlung in the chromosphere, here $\gamma_{ft} = \delta - 1$ (Brown 1971; Hannah & Kontar 2011). So, the acceleration and transport processes of FEBs can be well constrained if the HXR emissions from the corona source to the footpoint sources are both observable.

According to this simple scenario that the same FEBs produce the coronal source via thin-target bremsstrahlung and the footpoint sources via thick-target bremsstrahlung, the difference between the two photon spectral indices should be $\Delta\gamma = \gamma_{tp} - \gamma_{ft} = 2$ (Hannah & Kontar 2011; Holman et al. 2011; Simões & Kontar 2013). However, observations demonstrate that most flare events with the predicted spectral index difference are inconsistent with the standard model. Masuda et al. (2000) found a difference in spectral indices of the coronal and footpoint sources which were observed simultaneously for the first time by Masuda et al. (1994) with $\Delta\gamma < 2$. Petrosian et al. (2002) made a comprehensive analysis of 18 Yohkoh events and found that the spectral index of the coronal source is softer than that of footpoints on average by about 1. Battaglia & Benz (2006) analyzed five flares by examining the relation between coronal and footpoint sources and found that the average of all mean differences is about 1.8, and the differences of two events is larger than 2 and that of the other three events is smaller than 2. This inconsistency excludes the simple scenario that FEBs are freely propagating from the acceleration site to the footpoints and indicates that other transport effects must be considered.

On the other hand, the X-ray images with spectral capabilities enabled by Reuven Ramaty High Energy Solar Spectroscopic Imager (RHESSI) carry a wealth of information about the energetic electrons. One of the most important

findings by RHESSI is that many flares present a double power-law spectrum (Kontar et al. 2002; Conway et al. 2003; Holman et al. 2003). Furthermore, the spectral index of the double power-law photon spectrum at lower energy is usually smaller than that at higher energy. Various possible physical processes have been proposed to interpret the double power-law spectrum of HXR, such as (1) the inhomogeneous ionization along the path of FEBs (Brown 1973; Kontar et al. 2003; Su et al. 2011), (2) the instabilities of plasma (Holman et al. 1982; Melrose 1990; Hannah & Kontar 2011), (3) the photospheric albedo caused by Compton backscattering (Bai & Ramaty 1978; Jeffrey & Kontar 2011), (4) the acceleration process of energetic electrons (Lin & Hudson 1971) and (5) the energy losses (Holman et al. 1982; Alaoui & Holman 2017). The electron acceleration process or energy loss indicates that the energetic electrons have an initial broken power-law spectrum as they leave the acceleration site or they will evolve into such a double power-law distribution during propagation, respectively.

When FEBs travel in the solar atmosphere, they will lose part of their energy due to various energy loss mechanisms. In general, there are two main types of energy loss processes, the collisional energy loss due to Coulomb collisions with ambient plasma (Masuda et al. 2000; Petrosian et al. 2002; Zharkova & Gordovskyy 2006), and the noncollisional energy loss due to deceleration by induced electric fields. As presented by van den Oord (1990), an induced current (i.e., a return current) will be driven rapidly by the induced electric field and neutralize their carried ultrastrong beam current when FEBs travel along the magnetic field in the solar atmosphere. The energy of FEBs will inevitably be extracted by the induced electric field, which decelerates the FEBs. Numerous works have discussed the influence of induced current on FEBs and the ambient plasma (Emslie 1980, 1981; Zharkova & Gordovskyy 2006; Battaglia & Benz 2008; Holman 2012; Xu et al. 2013; Alaoui & Holman 2017). Considering the effects of return currents and collisions, Emslie (1980), Emslie (1981) studied the energy loss and heating rate of the power-law FEBs with a saturation low-energy cutoff behavior. Based on the analytic solution of the return current loss and an initial power-law FEB with a sharp cutoff behavior, Holman (2012) investigated the effect of the return current on the X-ray emission. Alaoui & Holman (2017) explained the breaks of the HXR spectrum around a few deka-keV with the return current model. They also adopted an initial power-law energy spectrum with a sharp cutoff behavior.

Observations demonstrate that the energy distribution of FEBs usually exhibits a power-law spectrum approximately, with a lower energy cutoff around deka-keV (Lin 1974; Bastian et al. 1998; Aschwanden 2002). It is difficult to identify the cutoff energy and the specific form of the cutoff behavior from observations. Therefore, as mentioned above, researchers often adopted extreme assumptions. One is the sharp cutoff behavior, that is $F(E) = 0$ for energies $E < E_c$, and the other is saturation

cutoff behavior, i.e., $F(E) = \text{constant} = F(E_c)$ for $E < E_c$. Here E_c is the cutoff energy which is much larger than the thermal energy of the ambient plasma T_e. In order to consider the effects of lower energy cutoff behavior on cyclotron maser emission, Wu & Tang (2008) fitted a more general lower-energy cutoff behavior of a power-law spectrum by relying on a hyperbolic tangent function

$$F(E) = A_b \tanh(E/E_c)^\delta (E/E_c)^{-\alpha}. \tag{1}$$

Here E denotes the energy of the energetic electrons, and A_b is the normalization factor. The lower-energy cutoff behavior of the power-law spectrum of the FEBs is described by a hyperbolic tangent function $\tanh(E/E_c)^\delta$, and δ and E_c are the steepness index and cutoff energy, respectively. α is the spectral index of the power-law spectrum. Wu & Tang (2008) showed that the lower-energy cutoff behavior will approach the sharp cutoff case if $\delta \gg \alpha$ and the saturation case if $\delta \leqslant \alpha$.

In a recent work, Tang et al. (2020) analyzed the parametric evolution of the power-law spectrum of FEBs traveling through a flare loop and discussed the possible effects on the associated HXRs and solar radio bursts (SRBs). They adopted the initial energy spectrum of FEBs as Equation (1). As mentioned above, active regions are characterized by ubiquitous loop structures. In addition to the flare loops, there are many coronal loops, which have a lower density and temperature than that of flare loops but higher than that of the ambient plasma. Due to the complex magnetic field structure of active regions, there are various burst events, such as emergence of magnetic flux, flares, filament eruptions and so on. Some of the accelerated electrons from these events travel in the flare loops, while the remaining accelerated electrons inevitably will propagate along the coronal loops. Although most coronal loops may not be rooted in the umbrae of sunspots, there are still many works that investigate whether coronal loops connect into sunspot umbrae. Foukal (1975) pointed out that the brightest coronal loops observed in the EUV band are associated with the flux tubes leading to sunspot umbrae. Several short-lived ($<$300 s), subarcsec bright dots have been observed above sunspots in addition to penumbrae in the transition region by Tian et al. (2014). According to Atmospheric Imaging Assembly (AIA) observations, they suggested that these bright dots are located at the base of loop structures. Straus et al. (2015) reported a burst of supersonic downflows above the lightbridge in a sunspot and interpreted their results as evidence of the termination shock in a cool umbral loop. Dammasch et al. (2008) indicated that the sunspot plumes are the common footpoints of several coronal loops. Because of the weak emission in the umbra, Chitta et al. (2016) reported on the umbral loops and traced them to their other footpoints, which were also rooted close to the umbra of the opposite polarity sunspot. In this paper, based on the semiempirical sunpot atmospheric model (Avrett et al. 2015), we investigate the parametric evolution of the FEBs during their propagation along coronal loops due to the energy losses. The rest of the paper is organized as follows. Section 2 introduces the sunpot atmospheric model and energy loss mechanisms. The energy loss and evolution of the energy spectrum of FEBs are presented in Section 3. Finally, a brief summary is given in Section 4.

2. Energy Loss Mechanisms and the Sunspot Atmospheric Model

2.1. Energy Loss Mechanisms

It is generally thought that HXR emission is attributed to bremsstrahlung. Flare-accelerated electrons propagate downwards along magnetic field lines into the denser chromosphere, then stop and heat the ambient plasma via Coulomb collisions (Brown 1971; Brown et al. 2003). These accelerated electrons of FEBs will lose their energy via interaction with the background dense plasma while they propagate in the coronal loops. There are two main types of energy loss mechanisms, i.e., collisional energy loss and noncollisional energy loss. Collisional energy loss is caused by Coulomb collisions with charged particles and neutral particles, and the noncollisional energy loss is due to deceleration by the induced electric field. The energy loss of the energetic electrons in FEBs is

$$\frac{dE}{dt} = \left(\frac{dE}{dt}\right)_{\text{coll}} + \left(\frac{dE}{dt}\right)_{\text{rc}}, \tag{2}$$

where the subscripts coll and rc indicate the energy loss by collision and deceleration of induced electric field, respectively. For hydrogen and helium solar plasma, neglecting the energy loss by protons and helium ions, and assuming that the speeds of FEBs are much greater than the mean speed of the background electrons, the collisional energy loss rate can be written as (Brown 1971; Emslie 1978; Holman et al. 2011)

$$\left(\frac{dE}{dt}\right)_{\text{coll}} = -\frac{2\pi e^4}{E} v[n_e \Lambda_{ee} + n_z(1 - \chi_z)\Lambda_{ez}]. \tag{3}$$

Here, e is the electronic charge, while E and v denote the energy and velocity of energetic electrons of FEBs, respectively. n_e and n_z are the number density of electrons and that of an element with atomic number Z in the ambient plasma, respectively. χ_z is the ionization rate of an element with atomic number Z. $\Lambda_{ee} \simeq ln(2E\lambda_D/e^2)$ is the Coulomb logarithm for electron-electron collisions, and $\Lambda_{ez} \simeq ln(2E/I_z)$ is the effective Coulomb logarithm for the interaction of a energetic electron with an atom. λ_D is the Debye length, and I_z is the ionization potential of a hydrogen or helium atom.

For the noncollisional energy loss rate, i.e., the energy loss via deceleration in the induced electric field, can be written as (Holman 2012)

$$\left(\frac{dE}{dt}\right)_{\text{rc}} = -eE_i v. \tag{4}$$

Here, E_i is the induced electric field driven by FEBs. In the steady state, according to Ohm's law, E_i can be derived as (Tang et al. 2020)

$$E_i = \frac{5.8 \times 10^{-5} n_b v_b (1 + \beta) m_e}{e T_e^{3/2}}. \tag{5}$$

Here n_b and v_b are the density and beam speed of FEBs, respectively. Parameter β is the excited level of ion-acoustic turbulence. m_e is the mass of an electron, and T_e is the temperature of background plasma in the unit of eV.

Noting that $vdt = -dh$, from Equations (3) and (4) we can obtain the total energy loss ΔE_j of beam electrons in the j-th layer from integral

$$\int_{E_{j-1}}^{E_j} EdE|_{\mathrm{coll}}$$
$$= -2\pi e^4 \int_{t_{j-1}}^{t_j} [n_e \Lambda_{ee} + (1 - \chi_z) n_z \Lambda_{ez}] vdt, \tag{6}$$

and

$$\int_{E_{j-1}}^{E_j} dE|_{\mathrm{rc}} = -\int_{t_{j-1}}^{t_j} e E_i v dt. \tag{7}$$

Here E_{j-1} and E_j are the energies of beam electrons at the top and bottom of the j-th layer, respectively. $l_j = h_{j-1} - h_j$ is the thickness of the j-th layer. If the density, temperature of background plasma and the induced electric field are approximated as constants in a single layer, the energy loss of the energetic electrons of FEBs can been obtained as

$$\Delta E_{\mathrm{coll}}^j = E_{j-1} - \sqrt{E_{j-1}^2 - 4\pi e^4 [n_e \Lambda_{ee} + (1 - \chi_z) n_z \Lambda_{ez}] l_j}, \tag{8}$$

and

$$\Delta E_{\mathrm{rc}}^j = e E_i l_j. \tag{9}$$

2.2. Sunspot Atmosphere Model

Although a lot of EUV and X-ray loops in the solar corona are not rooted in the sunspot umbrae, they still connect to the enhanced magnetic active region. Therefore, we believe that the plasma environment of the coronal loops is close to the sunspot atmosphere model. In this paper, we consider a semiempirical sunspot model proposed by Avrett et al. (2015). Compared with the flare model (Tang et al. 2020), the transition region of the sunspot atmosphere model is about 1000 km higher than that of the flare model. As mentioned in the Introduction, the temperature and density of the sunspot model are lower than those of the flare model, and the density is at least two orders of magnitude lower. Figure 1 plots the temperature and density distribution of the background plasma versus height h along the coronal loop. According to the sunspot model, we take the height of the loop top to be
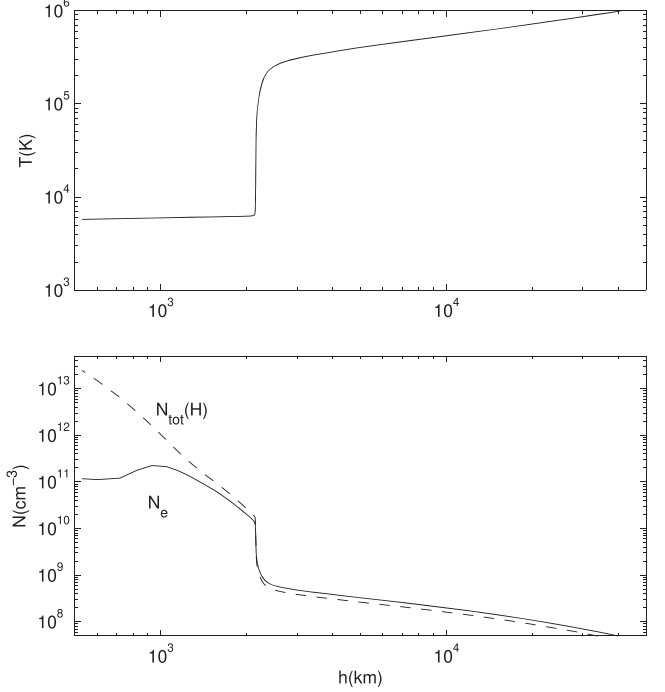

Figure 1. The temperature and density of background plasma as a function of height h along the coronal loop.

$h = 5.81 \times 10^4$ km. From the loop top to the bottom of the chromosphere (about 500 km), the coronal loop is divided into more than 90 layers. The height, temperature and density of the background plasma of each layer can be referred to in table 2 of Avrett et al. (2015). When calculating the energy loss of the FEBs in each layer with Equations (8) and (9) we assume that the temperature, density and induced electric field are constant in each layer, and we take these constants as the average values of the upper and lower boundaries of each layer.

3. Parametric Evolution of the Energy Spectrum of FEBs in Coronal Loops

As FEBs propagate downward along the coronal loops, the energetic electrons of FEBs will lose some of their energy due to Coulomb collisions and deceleration from the induced electric field. Based on the sunspot atmosphere model and Equations (8) and (9) we can calculate the energy loss $\Delta E = \Sigma_{j=1}^j \Delta E_j$ and the remaining energy E_j of the energetic electrons of FEBs when they arrive at a certain height h_j from the loop top. As mentioned above, observations from HXR and radio radiation demonstrate that the energy distribution of energetic electrons usually can be approximated by a negative power-law spectrum (Lin 1974; Aschwanden 2002), so the initial single power-law FEBs $F(E_0) \propto E_0^{-\delta}$ will evolve into a complex spectrum $F(E) \propto (E + \Delta E)^{-\delta}$ due to the energy loss ΔE. In the same way as Tang et al. (2020), we take the initial
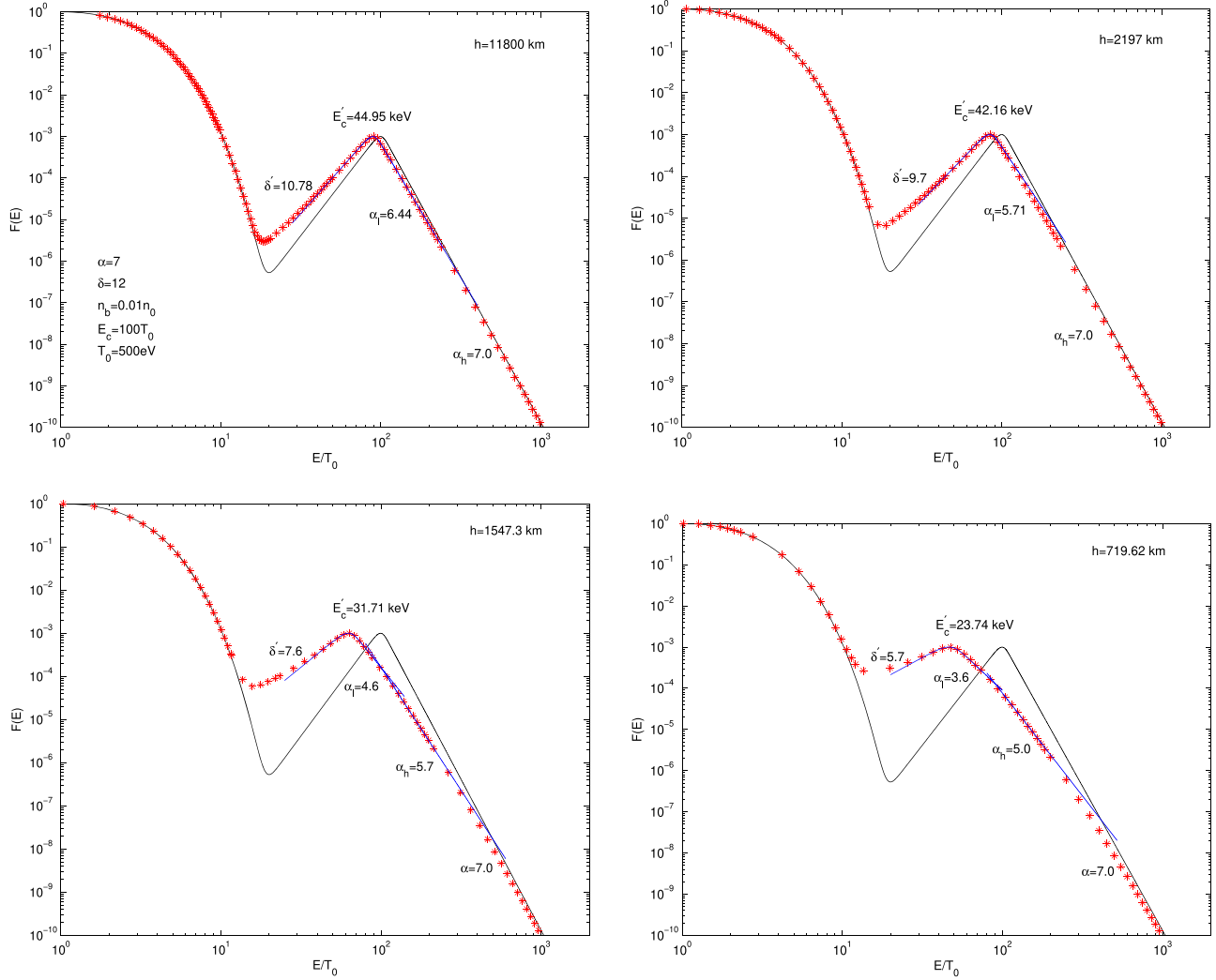
Figure 2. The evolution of the FEBs due to energy loss when traveling along the coronal loops and reaching heights $h = 11,800$ km, 2197 km, 1547.3 km and 719.62 km. Here, the cutoff energy $E_c = 50$ keV, steepness index $\delta = 12$ and spectral index $\alpha = 7$ of the initial FEBs. Ambient plasma temperature $T_0 = 500$ eV.

energy distribution function of FEBs as

$$F(E_0) = A_b \tanh\left(\frac{E_0}{E_c}\right)^{\delta}\left(\frac{E_0}{E_c}\right)^{-\alpha}, \qquad (10)$$

and at the looptop, it will evolve into the final form because of the energy loss ΔE

$$F(E) = A_b \tanh\left(\frac{E + \Delta E}{E_c}\right)^{\delta}\left(\frac{E + \Delta E}{E_c}\right)^{-\alpha}. \qquad (11)$$

Here, like in Equation (1), A_b is the normalization factor, the hyperbolic tangent function $\tanh(E_0/E_c)^{\delta}$ describes the lower-energy cutoff behavior and E_c is the cutoff energy. Since we only consider the energy change of the energetic electrons during their travel, the number of electrons with energy $E = E_0 - \Delta E$ in Equation (11) is equal to the number of

electrons with energy E_0 in Equation (10). That said, the energy distribution in Equation (11) is derived directly from the initial distribution Equation (10) in terms of the energy loss ΔE.

Figures 2–5 show the parametric evolution characteristics of the energy spectrum of FEBs propagating in the coronal loops. The four panels plot FEBs arriving at heights $h = 11,800$ km, 2197 km, 1547.3 km, and 719.62 km, respectively. The initial number density of energetic electrons of FEBs $n_b = 0.01n_e$ in Figures 2–4, and $n_b = 0.001n_e$ in Figure 5 have been used. The exciting level of ion-acoustic turbulence is assumed to $\beta = 10$ in the coronal and transition region, and $\beta = 0$ in the chromosphere. Here, the initial energy distribution of the FEBs is displayed as solid lines, which are superimposed on the thermal distribution of background plasma. The red stars signify the ultimate energy distribution of FEBs when they
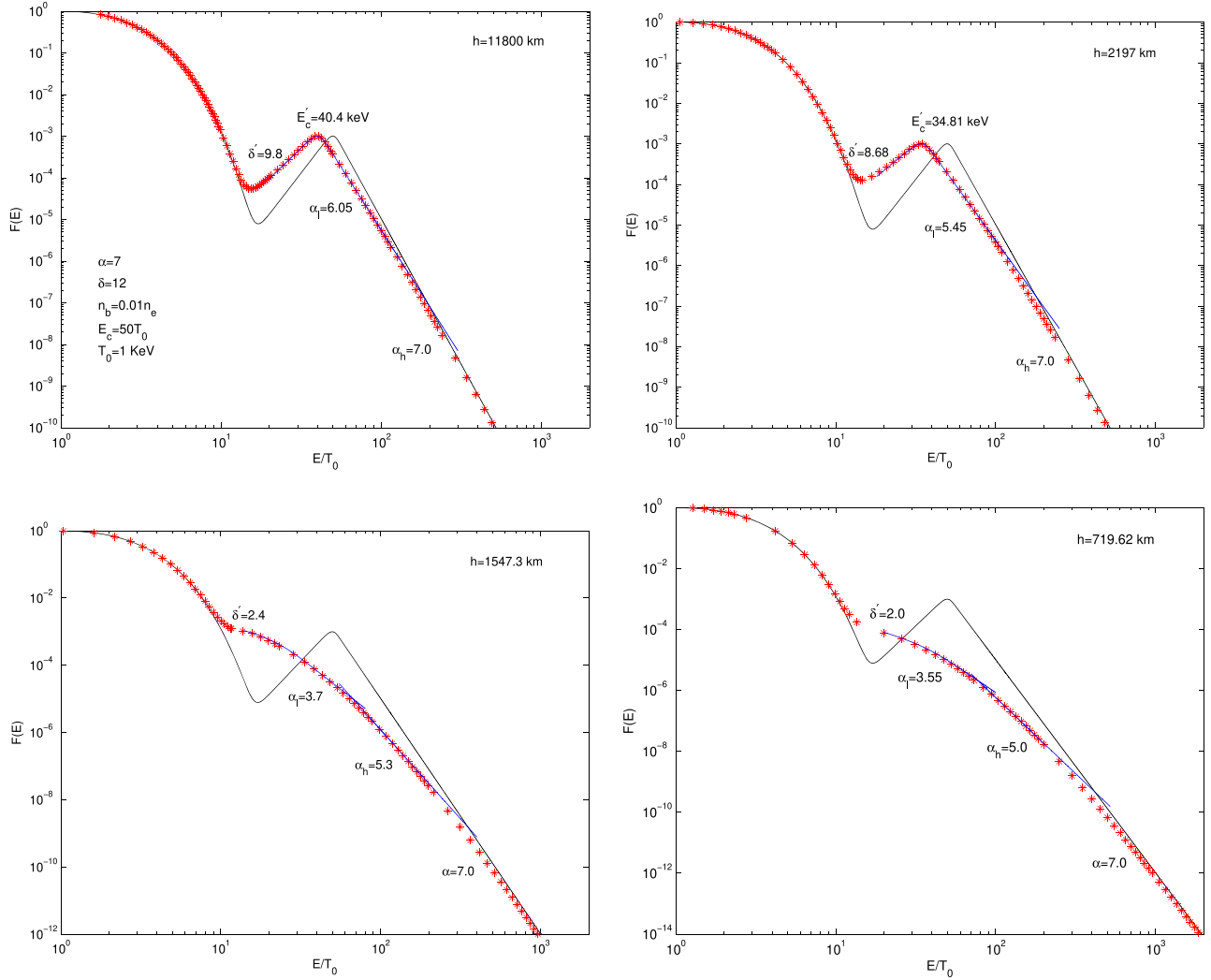
Figure 3. The evolution of the FEBs due to energy loss when traveling along the coronal loops reaches heights $h = 11{,}800$ km, 2197 km, 1547.3 km and 719.62 km. Here, the cutoff energy $E_c = 50$ keV, steepness index $\delta = 12$ and spectral index $\alpha = 7$ of the initial FEBs. Ambient plasma temperature $T_0 = 1$ keV.

arrive at a certain height. The blue lines are the fitting results with Equation (10) and power-law distribution.

In Figure 2, the initial power-law FEBs have the cutoff energy $E_c = 50$ keV, steepness index $\delta = 12$ and spectral index $\alpha = 7$. The temperature of background plasma $T_0 = 500$ eV has been used. The beam electrons lose some of their energy via Coulomb collisions and decelerate by the induced electric field when traveling along the coronal loops; the deeper the FEBs are precipitated, the more the electrons lose energy. Some of the energetic electrons will be thermalized and become the background electrons when they lose most of their energy. The lower energy cutoff behavior and the spectral characteristics of the FEBs will change significantly due to the energy loss ΔE being related to E_0. Figure 2 shows that the initial single power-law spectrum of FEBs will turn into a double power-law

spectrum or two knees power-law spectrum. The steepness cutoff behavior of FEBs will move toward lower energy and flatten out. From Figure 2, one can find that the cutoff energy E_c' and the steepness index δ' are about $E_c' = 44.95$ keV, $\delta' = 10.78$ at height $h = 11{,}800$ km, $E_c' = 42.16$ keV, $\delta' = 9.7$ at $h = 2197$ km, $E_c' = 31.71$ keV, $\delta' = 7.6$ at $h = 1547.3$ km, and $E_c' = 23.74$ keV, $\delta' = 5.7$ at $h = 719.62$ km, respectively. For the double power-law spectrum at $E > E_c'$ in the top two panels, we take the initial spectral index as the spectral indices of the higher energy part, i.e., $\alpha_h = 7.0$, and fit the spectral indices of the lower energy part α_l as $\alpha_l = 6.44$ and $\alpha_l = 5.71$. For the two knees power-law spectrum in the bottom two panels, we have the spectral indices $\alpha_l = 4.6$, $\alpha_h = 5.7$, $\alpha = 7.0$ at height 1547.3 km, and $\alpha_l = 3.6$, $\alpha_h = 5.0$, $\alpha = 7.0$ at 719.62 km, respectively.
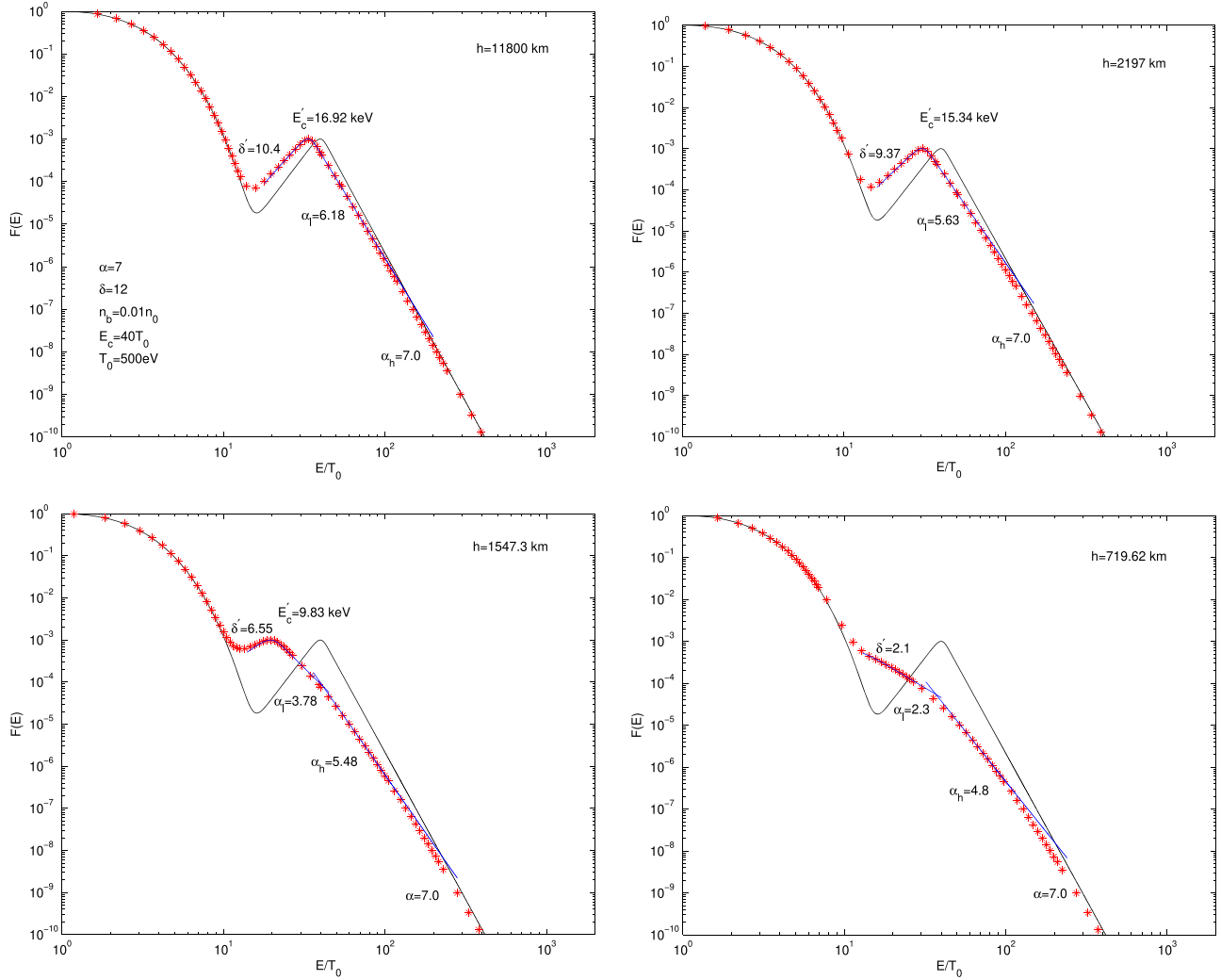
Figure 4. The evolution of the FEBs due to energy loss when traveling along the coronal loops reaches heights $h = 11{,}800$ km, 2197 km, 1547.3 km and 719.62 km. Here, the cutoff energy $E_c = 20$ keV, steepness index $\delta = 12$ and spectral index $\alpha = 7$ of the initial FEBs. Ambient plasma temperature $T_0 = 500$ eV.

In Figure 3, the temperature of ambient plasma $T_0 = 1$ keV, and parameters of the initial FEBs, such as the cutoff energy E_c, steepness index δ and spectral index α are the same as in Figure 2. Figure 3 also confirms that the energy spectrum and cutoff behavior of the initial FEBs have changed. The energy spectrum can be fitted with a double power-law spectrum at $h = 11{,}800$ and 2197 km, and a two knees power-law spectrum at $h = 1547.3$ km and 719.62 km. As the FEBs travel downward, the cutoff energy E_c also decreases and the steepness cutoff behavior finally turns into the saturation cutoff behavior. From Figure 3, one can find that the top two panels have the cutoff energies and steepness index $E_c' = 40.4$ keV, $\delta' = 9.8$, and $E_c' = 34.81$ keV, $\delta' = 8.68$, respectively. The spectral indices of the double power-law are $\alpha_l = 6.05$, $\alpha_h = 7.0$ at $h = 11{,}800$ km, and $\alpha_l = 5.54$, $\alpha_h = 7.0$ at

$h = 2197$ km, respectively, and the break energy is between $100 \sim 200$ keV. For the two knees power-law spectrum in the bottom panels of Figure 3, the spectral indices are $\alpha_l = 3.7$, $\alpha_h = 5.3$, $\alpha = 7.0$, and $\alpha_l = 3.55$, $\alpha_h = 5.0$, $\alpha = 7.0$, respectively. The two breaks are between $70 \sim 80$ keV and $300 \sim 400$ keV, respectively.

In Figure 4, the initial cutoff energy $E_c = 20$ keV has been used, but other parameters of initial FEBs and temperature of ambient plasma are the same as in Figure 2. From Figure 4, one can find that the steepness cutoff behavior becomes flat and the cutoff energy also decreases. It finally evolves into the saturation cutoff behavior in the last panel. The cutoff energy and steepness index are about $E_c' = 16.92$ keV, $\delta' = 10.4$ at $h = 11{,}800$ km, $E_c' = 15.34$ keV, $\delta' = 9.37$ at $h = 2197$ km, and $E_c' = 9.83$ keV, $\delta' = 6.55$ at $h = 1547.3$ km, respectively.
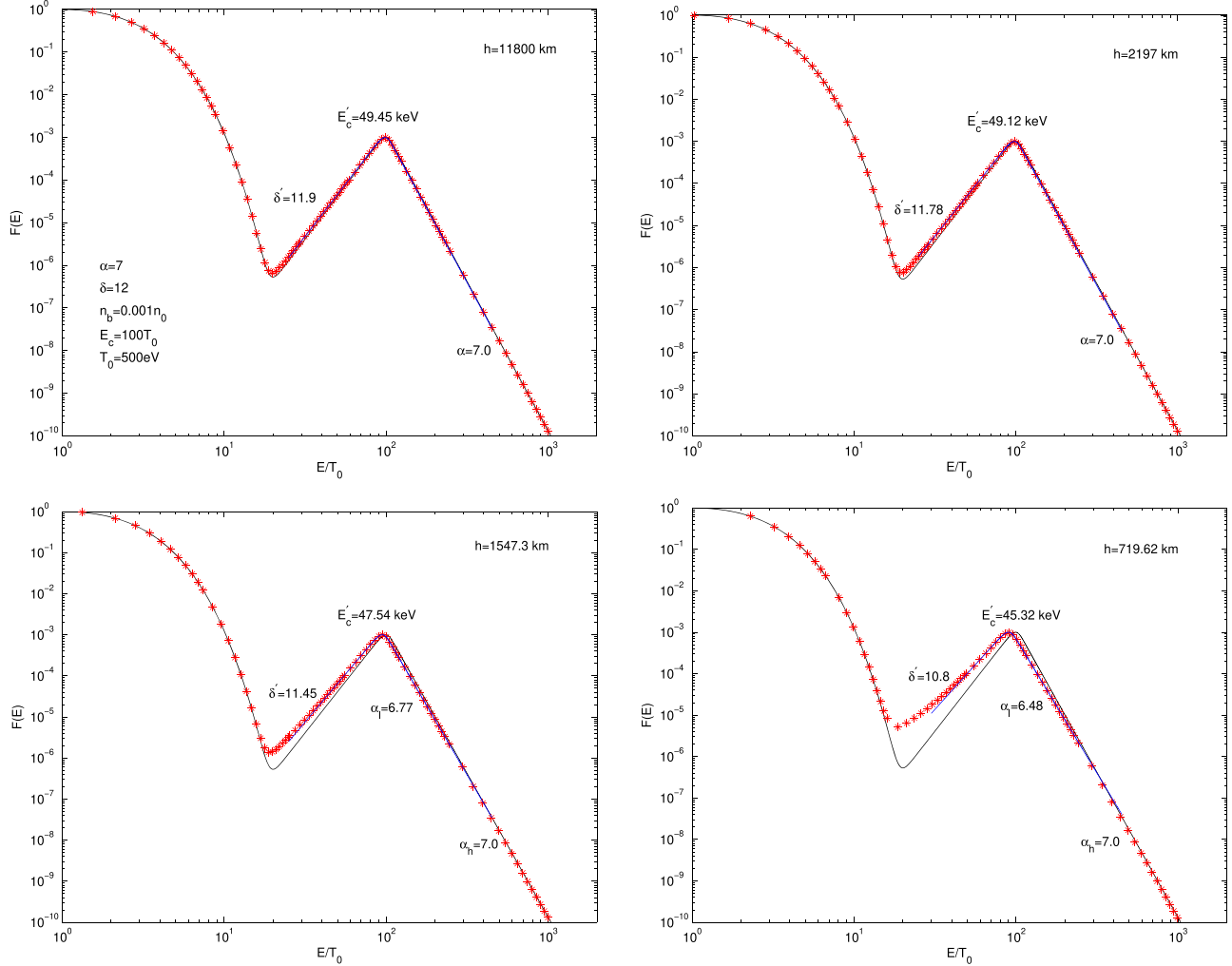
Figure 5. The evolution of the FEBs due to energy loss when traveling along the coronal loops reaches heights $h = 11{,}800$ km, 2197 km, 1547.3 km and 719.62 km. Here, the number density of the energetic electrons of FEBs $n_b = 0.001n_e$, and other parameters of the initial FEBS and ambient plasma are the same as in 2.

The top two panels in Figure 4 also affirm that the energy spectra can be well fitted with the double power-law spectrum. The spectral indices are $\alpha_l = 6.18$, $\alpha_h = 7.0$ and $\alpha_l = 5.63$, $\alpha_h = 7.0$ at heights $h = 11{,}800$ km and 2197 km, respectively, and the break energy is between 50 and 100 keV. For the two knees power-law spectrum at $h = 1547.3$ km and 719.62 km in the two bottom panels, the spectral indices are $\alpha_l = 3.78$, $\alpha_h = 5.48$, $\alpha = 7.0$, and $\alpha_l = 2.3$, $\alpha_h = 4.8$, $\alpha = 7.0$, respectively.

In Figure 5, the density of the energetic electrons of FEBs is taken to be $n_b = 0.001n_e$. Other parameters of the initial FEBs are $E_c = 50$ keV, $\delta = 12$ and $\alpha = 7$, and the temperature of the background plasma is $T_0 = 500$ eV. Due to the low density of the beam electrons, Figure 5 shows that the evolution of the energy spectrum of the FEBs is not significant. When the FEBs travel downward from the looptop to the chromosphere

footpoint along coronal loops, the low-energy cutoff behavior and the cutoff energy E_c are only slightly flattened and decrease. The cutoff energies are about $E_c' = 49.45$ keV, 49.12 keV, 47.54 keV and 45.32 keV, and the steepness indices are $\delta' = 11.9$, 11.78, 11.45 and 10.8 at $h = 11{,}800$ km, 2197 km, 1547.3 km and 719.62 km, respectively. One also can find from Figure 5 that the power-law energy spectrum of FEBs does not change significantly. The upper two panels still have a single power-law distribution, while the bottom two panels can be fitted with the double power-law spectrum. For the double power-law distribution at $h = 1547.3$ km and 719.62 km, the spectral indices are $\alpha_l = 6.77$, $\alpha_h = 7.0$, and $\alpha_l = 6.48$, $\alpha_h = 7.0$, respectively, and the difference between the two indices is inapparent.

Figure 6 plots the evolution of the cutoff energy E_c of the power-law spectrum of the FEBs when they precipitate along
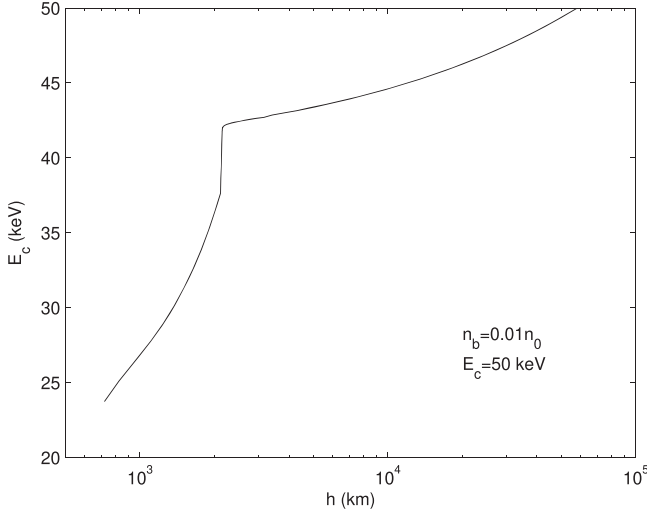
Figure 6. The evolution of the cutoff energy E_c of FEBs when traveling along the coronal loops, the parameters of the initial FEBs and ambient plasma are the same as in 2.

the coronal loops. Here, the initial parameters of FEBs as cutoff energy E_c and number density n_b, the excited level of ionacoustic turbulence β and the ambient plasma parameters are the same as in Figure 2. As FEBs propagate downwards along the coronal loops, Figure 6 clearly demonstrates that the cutoff energy E_c decreases slowly at first, and then decreases rapidly when the FEBs reach the transition region. This indicates the higher energy loss rate in the transition region and chromosphere than in the corona.

4. Summary and Conclusion

Energetic electrons are ubiquitous in space and cosmic plasmas. For the Sun, energetic electrons are usually accelerated by the magnetic reconnection process of flares or by a corona shock wave. A typical large solar flare, for example, can release huge amounts of magnetic energy of about 10^{30}–10^{33} erg in a short period of time (Hudson 2011). The rapid release of magnetic energy causes a large number of particles to be accelerated to a high energy state in a short time. Accelerated electrons travel along the magnetic field lines in the solar atmosphere and emit radiation from $\gamma-$ray to radio emission. It is generally believed that when FEBs propagate in the magnetic field, they will produce radio radiation (such as type III bursts) and HXR emission. The former is usually generated by the plasma emission mechanism or cyclotron maser emission mechanism, and the latter is generated via bremsstrahlung due to the electrons with small pitch angles that precipitate into the denser chromosphere. High-resolution observations of HXR and radio emission can provide a wealth of information about the physics of acceleration and

propagation of FEBs. As Holman et al. (2011) point out, the location where FEBs emit radiation is not necessarily where they are accelerated. Some puzzles remain, such as the inconsistency of the index difference between the traditional thin-thick target X-ray model with observations (Hannah & Kontar 2011; Holman et al. 2011), the difficult to explain spectrum break (Alaoui & Holman 2017) and the so-called particle number problem (Brown 1972) required to extend the interpretation of X-ray emission from the purely collisional energy loss to consideration of noncollisional energy losses due to the deceleration in the induced electric field.

Tang et al. (2020) studied the evolution of the energy spectrum of the FEBs and discussed the possible effects on the HXRs and radio radiation as FEBs traveling through the flare loops. Observations from X-ray and EUV show that solar active regions are almost composed of loop structures which are connected to the enhanced magnetic active region. A flare loop is one type of the coronal loop and has the highest temperature and density. As mentioned earlier, in addition to flare loops, there are many coronal loops with low temperature and density. Therefore, we believe that some of the accelerated electrons will inevitably enter and travel along the coronal loops. In this paper, we consider power-law injected FEBs as Tang et al. (2020) did and investigate their evolution due to the energy loss as propagating along the coronal loops.

As Tang et al. (2020) presented, the energy loss of beam electrons will change the energy spectrum distribution of FEBs when propagating in flare loops. Our results also consider the evolution of the energy spectrum of FEBs, but it becomes much weaker in coronal loops than in flare loops. In Figure 5, the parameters of initial FEBs and ambient plasma are consistent with Figure 3 of Tang et al. (2020), but the low-energy cutoff behavior and the cutoff energy E_c of FEBs are only slightly flattened and decrease as they travel from looptop down to the chromosphere. In view of the fact that the plasma density of the coronal loop is 1–2 orders of magnitude lower than that of the flare loop, the density ratio parameter n_b/n_0 in the coronal loop should be 1–2 orders of magnitude higher, assuming that the number of energetic electrons entering the coronal loop and flare loop is comparable. So, we take the density ratio $n_b/n_0 = 0.01$ in Figure 2–4. Similar to Tang et al. (2020), our calculations demonstrate that the steepness cutoff behavior of FEBs will be flattened and even turn into the saturation cutoff behavior, and the single power-law spectrum of initial FEBs can evolve into a double power-law spectrum or a two knees power-law spectrum when precipitating at a certain height. These evolution results of the energy spectrum of FEBs will also cause the corresponding observational effects in HXR and radio emissions.

As mentioned above, the FEB spectrum can be inferred from the photon spectrum of HXR based on the bremsstrahlung mechanism. The most important feature of the FEB spectrum is that it usually exhibits a double power-law spectrum

(Lin & Schwartz 1987; Dulk et al. 1992; Kontar et al. 2002; Conway et al. 2003; Holman et al. 2003; Chen et al. 2021). Lin & Schwartz (1987) reported a well fitted double power-law HXR spectrum in the impulsive phase of the 1980 June 27 flare, and the break knee is between 25 and 60 keV. Dulk et al. (1992) investigated 93 HXR flares and found that almost all the HXR spectra would break down into a double power-law spectrum at about 100 keV when reaching the peak emission. The difference in spectral indices between the lower and higher energy parts is about $1 - 2$. By combining the HXR and microwave observations, Chen et al. (2021) studied an X8.2 limb flare on 2017 September 10 and derived the energetic electron distribution of the source in the impulsive phase. They also fitted the nonthermal tail from ~ 16 keV as a double power-law spectrum, which breaks down at ~ 160 keV with the spectral indices ~ 3.6 below and >6.0 above the break energy. Although many physical mechanisms have been proposed to interpret the double power-law spectrum of energetic electrons, the energy loss process cannot be ignored. Our calculation results show that the initial single power-law spectrum of FEBs can evolve into the double power-law or two knees power-law spectrum (Figures 2–4). The difference in spectral indices of the power-law spectrum below and above the break energy is about $1 - 2$, and the break energy is between tens to hundreds of keV. We believe that such a double power-law distribution of FEBs can produce the break power-law HXR spectra as Dulk et al. (1992), and Chen et al. (2021) observed.

The very similar temporal behavior between HXR and SRBs indicates that they have a common nonthermal source, FEBs. Therefore, the spectral indices of the two emissions should be correlated directly. However, a lot of previous studies indicate that the spectral indices of FEBs derived from microwave and HXR observations are usually different (Kundu et al. 1994; Silva et al. 2000; Asai et al. 2007, 2013). This is attributed to the fact that microwave emission is mainly dominated by electrons above 300 keV, whereas HXR radiation is sensitive to electrons with tens of keV (White et al. 2011). So, it is desirable to have HXR emission up to several hundred keV when comparing the spectral indices deduced from these two emissions. Some studies have found that the radio-deduced and HXR-deduced spectral indices are compatible at energies above several hundred keV (Trottet et al. 1998; Vilmer et al. 1999; da Silva & Valio 2021). This is consistent with our results qualitatively. Because of the energy loss of energetic electrons, which is dependent on the initial energy, the FEBs will evolve into a double or two knees power-law spectrum when precipitating along the coronal loops. The break energy that separates the two power-law parts is between tens and hundreds of keV (Figures 2–4). We can find from these figures that the spectral indices of the lower-energy parts are $1 - 2$ lower than those of high-energy parts (above several hundred keV), while the spectral indices of the high-energy parts hardly change during their propagation. This may explain why there is

usually a discrepancy between spectral indices deduced from HXRs (low energy) and radio emissions, while having comparable spectral indices when HXRs are at energies above several hundred keV.

The lower energy cutoff behavior of FEBs can provide free energy for electron cyclotron maser emission (ECME). Our results show that the initial steepness cutoff behavior of FEBs will flatten and even turn into a saturation cutoff behavior. One can expect the possible effects of these evolving FEBs on the radio emission excited by ECME. Tang et al. (2016) roughly studied the ECME growth rates of evolving FEBs due to energy loss and the variation of ambient plasma parameters when traveling in the solar atmosphere. They found that the evolution of FEBs has a prominent influence on the ECME and hence the burst types of SRBs. In this paper, we do not consider the influence of other factors on the evolution of the FEB spectrum. Further elaboration and systematic investigation are needed.

Acknowledgments

References

Alaoui, M., & Holman, G. D. 2017, ApJ, 851, 78
Asai, A., Kiyohara, J., Takasaki, H., et al. 2013, ApJ, 763, 87
Asai, A., Nakajima, H., Oka, M., Nishida, K., & Tanaka, Y. T. 2007, AdSpR, 39, 1398
Aschwanden, M. J. 2002, SSRv, 101, 1
Aschwanden, M. J., Benz, A. O., Dennis, B. R., & Schwartz, R. A. 1995, ApJ, 455, 347
Avrett, E., Tian, H., Landi, E., Curdt, W., & Wülser, J. P. 2015, ApJ, 811, 87
Bai, T., & Ramaty, R. 1978, ApJ, 219, 705
Bastian, T. S., Benz, A. O., & Gary, D. E. 1998, ARA&A, 36, 131
Battaglia, M., & Benz, A. O. 2006, A&A, 456, 751
Battaglia, M., & Benz, A. O. 2008, A&A, 487, 337
Brown, J. C. 1971, SoPh, 18, 489
Brown, J. C. 1972, SoPh, 26, 441
Brown, J. C. 1973, SoPh, 28, 151
Brown, J. C., Emslie, A. G., & Kontar, E. P. 2003, ApJL, 595, L115
Chen, B., Battaglia, M., Krucker, S., Reeves, K. K., & Glesener, L. 2021, ApJL, 908, L55
Chitta, L. P., Peter, H., & Young, P. R. 2016, A&A, 587, A20
Conway, A. J., Brown, J. C., Eves, B. A. C., & Kontar, E. 2003, A&A, 407, 725
da Silva, D. F., & Valio, A. 2021, ApJL, 915, L1
Dammasch, I. E., Curdt, W., Dwivedi, B. N., & Parenti, S. 2008, AnGeo, 26, 2955
Del Zanna, G., & Mason, H. E. 2003, A&A, 406, 1089
Dulk, G. A., Kiplinger, A. L., & Winglee, R. M. 1992, ApJ, 389, 756
Emslie, A. G. 1978, ApJ, 224, 241
Emslie, A. G. 1980, ApJ, 235, 1055
Emslie, A. G. 1981, ApJ, 249, 817
Foukal, P. 1975, SoPh, 43, 327

Hannah, I. G., & Kontar, E. P. 2011, A&A, 529, A109
Hara, H., Watanabe, T., Harra, L. K., Culhane, J. L., & Young, P. R. 2011, ApJ, 741, 107
Holman, G. D. 2012, ApJ, 745, 52
Holman, G. D., Aschwanden, M. J., Aurass, H., et al. 2011, SSRv, 159, 107
Holman, G. D., Kundu, M. R., & Papadopoulos, K. 1982, ApJ, 257, 354
Holman, G. D., Sui, L., Schwartz, R. A., & Emslie, A. G. 2003, ApJL, 595, L97
Holt, S. S., & Cline, T. L. 1968, ApJ, 154, 1027
Hudson, H. S. 2011, SSRv, 158, 5
Imada, S., Aoki, K., Hara, H., et al. 2013, ApJL, 776, L11
Jeffrey, N. L. S., & Kontar, E. P. 2011, A&A, 536, A93
Kontar, E. P., Brown, J. C., Emslie, A. G., et al. 2003, ApJL, 595, L123
Kontar, E. P., Brown, J. C., & McArthur, G. K. 2002, SoPh, 210, 419
Kundu, M. R., White, S. M., Gopalswamy, N., & Lim, J. 1994, ApJS, 90, 599
Lin, R. P. 1974, SSRv, 16, 189
Lin, R. P. 2011, SSRv, 159, 421
Lin, R. P., & Hudson, H. S. 1971, SoPh, 17, 412
Lin, R. P., & Hudson, H. S. 1976, SoPh, 50, 153
Lin, R. P., & Schwartz, R. A. 1987, ApJ, 312, 462
Masuda, S., Kosugi, T., Hara, H., Tsuneta, S., & Ogawara, Y. 1994, Natur, 371, 495
Masuda, S., Sato, J., Kosugi, T., & Sakao, T. 2000, AdSpR, 26, 493

Melrose, D. B. 1990, SoPh, 130, 3
Narukage, N., Shimojo, M., & Sakao, T. 2014, ApJ, 787, 125
Petrosian, V., Donaghy, T. Q., & McTiernan, J. M. 2002, ApJ, 569, 459
Reale, F. 2010, LRSP, 7, 5
Schrijver, C. J., Title, A. M., Berger, T. E., et al. 1999, SoPh, 187, 261
Silva, A. V. R., Wang, H., & Gary, D. E. 2000, ApJ, 545, 1116
Simões, P. J. A., & Kontar, E. P. 2013, A&A, 551, A135
Straus, T., Fleck, B., & Andretta, V. 2015, A&A, 582, A116
Su, Y., Holman, G. D., & Dennis, B. R. 2011, ApJ, 731, 106
Syrovatskii, S. I., & Shmeleva, O. P. 1972, SvA, 16, 273
Tan, B., Chen, N., Yang, Y.-H., et al. 2019, ApJ, 885, 90
Tang, J. F., Wu, D. J., Chen, L., Xu, L., & Tan, B. L. 2020, ApJ, 904, 1
Tang, J. F., Wu, D. J., Chen, L., Zhao, G. Q., & Tan, C. M. 2016, ApJ, 823, 8
Tian, H., Kleint, L., Peter, H., et al. 2014, ApJL, 790, L29
Trottet, G., Vilmer, N., Barat, C., et al. 1998, A&A, 334, 1099
van den Oord, G. H. J. 1990, A&A, 234, 496
Vilmer, N., Trottet, G., Barat, C., et al. 1999, A&A, 342, 575
White, S. M., Benz, A. O., Christe, S., et al. 2011, SSRv, 159, 225
Wu, D. J., & Tang, J. F. 2008, ApJL, 677, L125
Xu, L., Chen, L., & Wu, D. J. 2013, A&A, 550, A63
Yokoyama, T., Akita, K., Morimoto, T., Inoue, K., & Newmark, J. 2001, ApJL, 546, L69
Zharkova, V. V., & Gordovskyy, M. 2006, ApJ, 651, 553